Advanced Optical Materials

ADVANCED OPTICAL MATERIALS
www.advopticalmat.de

RESEARCH ARTICLE OPEN ACCESS

Controlling Ultrafast Photonic-Plasmonic Coupling in a Hybrid Platform for Biosensing Applications

Diego Florio[1,2] | Andrea Chiappini[3] | Laura Pasquardini[4,5] | Mario Barozzi[6] | Monica Bollani[1] | Salvatore Stagira[2] | Tersilla Virgili[1]

[1]Istituto di Fotonica e Nanotecnologia, Consiglio Nazionale delle Ricerche (CNR), Piazza Leonardo da Vinci 32, Milano Italy, Milano, Italy | [2]Dipartimento di Fisica, Politecnico di Milano, Milano, Italy | [3]Istituto di Fotonica e Nanotecnologia, Consiglio Nazionale delle Ricerche (CNR) and FBK Photonics Unit, Povo, Trento, Italy | [4]Indivenire srl, Trento, Italy | [5]Department of Engineering, University of Campania Luigi Vanvitelli, Aversa, Italy | [6]Sensors and Devices, Fondazione Bruno Kessler, Trento, Italy

Correspondence: Diego Florio (diego.florio@polimi.it) | Andrea Chiappini (andrea.chiappini@cnr.it) | Tersilla Virgili (tersilla.virgili@cnr.it)

Received: 24 November 2025 | **Revised:** 5 March 2026 | **Accepted:** 6 March 2026

Keywords: biosensing | photonic crystals | plasmon resonance | ultrafast spectroscopy

ABSTRACT

Photonic crystals (PhCs) are attractive for several applications due to their ability to confine light and enhance near-field interactions at low fabrication cost. Their optical response is characterized by the presence of a photonic bandgap (PBG). When combined with plasmonic nanostructures supporting localized surface plasmon resonances (LSPRs), they form metal–dielectric hybrids (MDHs) with enhanced and tunable optical functionalities. Here, we fabricate an MDH featuring gold nanocaps (NCs) on the surface of a colloidal PhC (opal) and characterize its optical response using static and femtosecond transient absorption (TA) spectroscopy. Static measurements reveal a broad plasmonic resonance, arising from the LSPRs sustained by the gold NCs. TA measurements uncover a strong interplay between the metal LSPRs and the opal PBG: the plasmon transient response is significantly enhanced by the PBG. For the first time, to the best of our knowledge, we demonstrate that this enhancement can be controlled by varying the excitation wavelength, owing to the slow-light regime, in agreement with the transfer matrix model predictions. Moreover, we show as proof-of-concept that the MDH ultrafast optical response is significantly modified by bacterial deposition, enabling ultrafast switching of the transient signal and underscoring the potential of these devices for biosensing applications.

1 | Introduction

The ability to precisely manipulate light at the nanoscale has emerged as a fundamental pillar of modern nanoscience and photonics [1–3]. Nanoscale control of light is essential not only for realizing the next generation of compact, high-performance optical devices capable of processing information at unprecedented speeds [4], but also for developing highly sensitive and tunable optical sensors [5, 6]. Over the past decades, two seemingly distinct classes of materials have emerged as central to nanophotonic applications: photonic crystals (PhCs) and plasmonic metal nanostructures. PhCs exploit periodic arrangements of dielectric elements, such as nanospheres, that produce a well-defined spatial modulation of the refractive index. The periodicity of PhCs influences light propagation in a manner analogous to how the atomic lattice in semiconductors governs electron motion [7]. When an electromagnetic wave interacts with a PhC, multiple interferences between forward- and backward-propagating

Diego Florio and Andrea Chiappini contributed equally to the work.

diffracted waves give rise to peculiar forbidden frequency ranges where destructive interference dominates, known as photonic bandgaps (PBGs) [8, 9]. The spectral position of the PBGs is directly related to the PhCs nanosphere diameter, which is a tunable fabrication parameter, thus offering a convenient platform for light control at the nanoscale.

The second class of materials that have been widely studied and exploited for nanophotonics is represented by metal nanostructures. [10–12]. In a metal, the free electrons can oscillate collectively in states known as plasmons, once they are excited with electromagnetic waves resonant with the plasmonic modes. While the plasmonic frequency in bulk metals depends primarily on intrinsic material properties, size reduction to the nanoscale introduces new localized surface plasmon modes, arising from the confinement of the electron oscillations at the surface. These modes allow light to be confined and manipulated on spatial scales much smaller than its wavelength, thereby overcoming the classical diffraction limit. The resulting electromagnetic field enhancement leads to intense localized fields in subwavelength volumes, dramatically amplifying light–matter interactions [13, 14]. The resonance frequency of these localized plasmons is highly sensitive to the geometry, size, and aspect ratio of the nanostructures, offering versatile control for device design across diverse photonic applications.

Although both photonic crystals and plasmonic nanostructures enable powerful manipulation of light, each approach faces inherent limitations. In fact, photonic crystals struggle to confine light below the diffraction limit, while plasmonic nanostructures suffer from strong optical losses, factors that have historically restricted their integration into fully scalable nanophotonic systems [15, 16].

A promising approach involves the development of hybrid metal-dielectric structures, where the coexistence of plasmonic and photonic properties is not merely additive; rather, their coupling gives rise to powerful and novel optical modes [17, 18]. Numerous examples of hybrid systems combining photonic crystals and metallic components have been reported in the literature. Their optical properties have been extensively studied across different dimensionalities (1D, 2D, and 3D), metallic materials and geometry such as planar films, nanoparticles, nano-islands, and corrugated films, primarily through static measurements. [19–27].

Among these systems, 3D PhCs, also known as colloidal crystals, coupled with metallic nanostructures, have shown great potential as sensing platforms. Their sensing capability arises from the enhancement of Raman signals or changes in static transmittance and reflectance spectra upon analyte binding. For example, Guddala et al. [28] demonstrated that an inverse colloidal crystal decorated with gold nanoparticles can enhance the Raman scattering of benzenethiol. Similarly, colloidal metal–dielectric Surface Enhanced Raman Spectroscopy (SERS) substrates have been shown to detect both small molecules and microorganisms [29], while silver-coated 3D PhCs can sense Rabbit IgG down to 134 pM [30]. A gold–aluminum colloidal photonic crystal with solvent-tunable structural color has also been developed for advanced anti-counterfeiting applications [31].

Beyond static optical characterization, ultrafast time-resolved spectroscopy in pump–probe geometry has been used to investigate the ultrafast optical and electronic dynamics in hybrid colloidal plasmonic–photonic crystals (HCPPC) [32, 33]. The temporal resolution available with ultrafast time-resolved spectroscopy allows to reveal key phenomena, including plasmon relaxation, energy transfer between metal and dielectric components, and transient shifts in the PBG [34]. Understanding these femtosecond-to-picosecond dynamics is crucial for the design of advanced nanophotonic devices, including ultrafast optical switches [35, 36] and enhanced SERS substrates.

Here, we investigate the optical properties of a HCPPC using steady-state and femtosecond transient absorption spectroscopy. Experiments were conducted using different excitation wavelengths and probing angles to investigate the system's dynamic behavior. For the first time, to the best of our knowledge, we reveal a twofold enhancement of the plasmonic transient signal when it spectrally overlaps with the PBG, which, due to the slow-light regime, can be controlled by adjusting the excitation wavelength, in agreement with predictions from a transfer matrix model (TMM). Furthermore, the sensitivity of the hybrid structure to its environment was demonstrated as proof-of-concept through bacterial deposition, which strongly modifies the ultrafast response, highlighting the potential of HCPPCs for biosensing and ultrafast photonic switching.

2 | Results and Discussion

2.1 | Sample Characteristics

The HCPPC investigated in this study incorporates a 3D photonic crystal composed of an 8 μm-thick opal structure. This structure is fabricated by the self-assembly of a monodisperse colloidal solution containing silica nanospheres with a diameter (D) of 290 nm (Opal), deposited vertically onto a fused silica substrate. A nominal 20 ± 5 nm-thick gold layer is then deposited on the opal surface via e-beam evaporation. From now on, this sample will be referred to as Opal/Au. To serve as a reference for characterizing the plasmonic properties of the gold layer, an identical gold evaporation is directly performed onto a separate fused silica substrate, producing an Au film. The schematics of the fabrication processes for both the Au film and the Opal/Au hybrid are shown in Figure 1a,b, respectively.

Interestingly, the metal deposition formed on the opal surface of the Opal/Au hybrid assumes a peculiar morphology, made by gold nanocaps (NC) connected by a thin film, as observed via a high-resolution scanning electron microscopy (SEM) image shown in Figure 1c (see Figure S1 for higher magnification). This nano-structuring follows an ordered pattern inherited from the periodicity of the opal surface. Moreover, within the interstitial spaces between opal spheres subwavelength size holes form.

2.2 | Static Optical Properties

Figure 1d shows the transmittance spectra in the visible-NIR range of Au film, Opal, and Opal/Au samples, in yellow, grey, and dark red, respectively. The Au film transmittance shows a

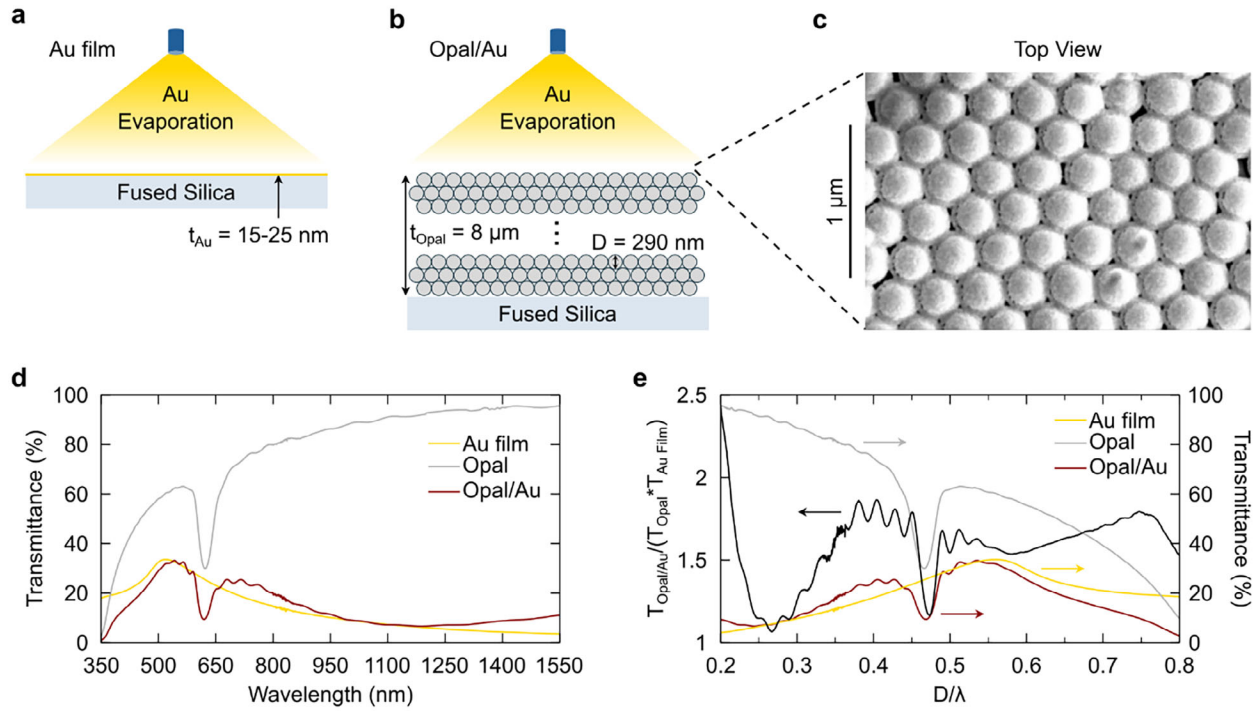

FIGURE 1 | (a) Schematic of Au film deposition via e-beam evaporation, yielding a nominal 20 nm thick film on a fused silica substrate. (b) Schematic of Au deposition via e-beam evaporation on 8 μm-thick artificial opal structure, self-assembled from 290 nm diameter silica spheres on a fused silica substrate. (c) SEM planar view image of the top surface of the Opal/Au hybrid. (d) Transmittance spectra of the Au film (yellow), Opal (grey), and Opal/Au hybrid (dark red). (e) Reduced transmittance spectrum of Opal/Au hybrid normalized to the Opal and Au film transmittance (black). Transmittance spectra of the Au film (yellow), Opal (grey), and Opal/Au hybrid (dark red).

peak at ≈500 nm corresponding to the onset of the intra-band transitions within the conduction band. The Opal transmittance is dominated by the PBG at ≈625 nm. In the Opal/Au hybrid, the presence of the highly reflective gold layer reduces transmittance across the entire spectral range investigated. However, light is not entirely prevented from diffracting through the depth of the 3D opal, allowing the PBG structure to be preserved, though it exhibits a slight blueshift.

Notably, the transmittance spectrum of the Opal/Au hybrid does not result from a simple superposition of the spectral features of the individual components. Figure 1e presents the transmission of the Au film (yellow line), the Opal (grey line) and the Opal/Au hybrid (red line) as a function of the reduced frequency D/λ, where D is the opal nanosphere diameter that in our case is 290 nm. Figure 1e also shows the Opal/Au transmission spectrum normalized to the transmission of both components (black line). Representing the data in terms of the reduced frequency D/λ allows for a direct comparison of the optical responses of different hybrid opal structures with varying periodicities. In fact, spectral features that depend on the diameter of the nanospheres composing the opal structure align at the same position in the spectrum, whereas those depending on other structural parameters can appear at different spectral positions [17].

In the normalized Opal/Au transmission spectrum, we observe several specific features having distinct origins. First, we note an extraordinary transmission band around D/λ = 0.77 (λ = 377 nm for D = 290 nm) which has been assigned to the reirradiation of surface plasmon polariton waves excited at the metal-dielectric interface via diffractive coupling within the opal. [17, 37]. The observed intensity is relatively low, likely due to the intrinsic absorption of gold at these wavelengths. Nevertheless, its presence suggests that the opal structure acts as a coupler that partially compensates for metallic losses.

Second, we observe transmission passbands in the range D/λ = 0.25–0.55, related to the enhancement of opal Fabry-Pérot oscillations due to coupling to the plasmonic coating. [17] Third, the spectrum reveals a broad transmission dip centered at around D/λ = 0.26 (λ = 1100 nm), which can be attributed to reflection and absorption arising from a broad localized surface plasmon resonance (LSPR) supported by the metallic NCs shown in Figure 1c. These resonances do not show angular dispersion, and their spectral characteristics depend on fabrication parameters such as the metal deposition angle and thickness, as well as the diameter of the opal spheres, which together determine the aspect ratio of the plasmonic nanostructures. [17, 26] For small sphere diameters (100–300 nm) and thin metal coatings (tens of nanometers), the LSPRs are expected to lie within the visible-NIR spectral range, in agreement with our experimental observations. [17, 38, 39].

2.3 | Transient Optical Properties

Femtosecond transient absorption (TA) spectroscopy offers a valuable complement to static transmittance measurements, providing dynamic insight into the possible coupling effects between

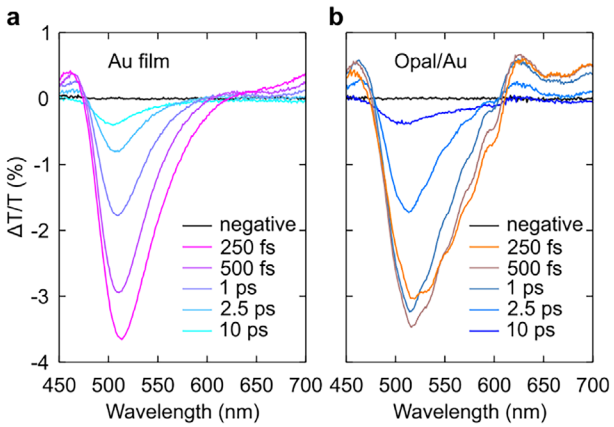

FIGURE 2 | TA spectra at different pump-probe delays for the Au film (a) and for Opal/Au hybrid (b), following 400 nm excitation.

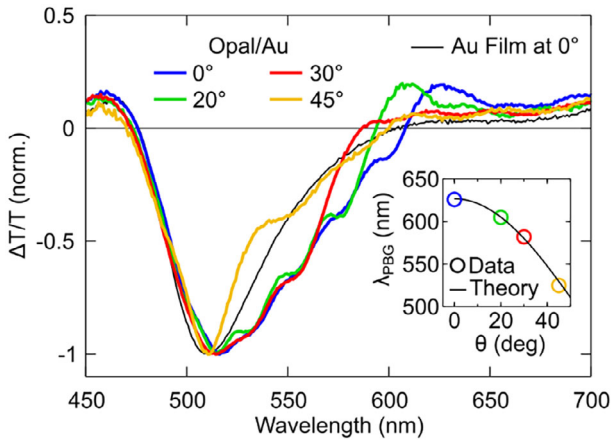

FIGURE 3 | TA spectra at 500 fs pump–probe delay after 400 nm excitation of the Opal/Au hybrid, normalized to the minimum, for vertically polarized probe incident at 0° (blue), 20° (green), 30° (red), and 45° (dark yellow), and of the Au film (black). Inset: Incident-angle dependence of the PBG spectral position in the static transmittance of the Opal/Au hybrid. Experimental data are shown as colored circles matching the corresponding spectra, while the theoretical angular dispersion of the PBG is represented by the black line.

the photonic and plasmonic modes, and revealing how these interactions influence the photophysics of the gold layer. All measurements are discussed in terms of the relative differential probe transmission change:

$$\frac{\Delta T}{T}(\lambda,\tau) = \frac{T_{ON}(\lambda,\tau) - T_{OFF}(\lambda)}{T_{OFF}(\lambda)} \quad (1)$$

where $T_{ON}(\lambda,\tau,)$ and $T_{OFF}(\lambda)$ are the transmitted (T) probe spectra with and without the optical pump, respectively, and τ is the pump-probe delay. Further details can be found in the "Femtosecond transient absorption spectroscopy" Experimental section.

Figure 2 shows the TA spectra of the Au film and the Opal/Au hybrid samples as a function of pump–probe delay following 400 nm excitation. Distinct spectral signatures appear in the hybrid sample that are absent in the pure Au film. For the Au film (Figure 2a), excitation at 400 nm predominantly triggers strong interband electronic transitions. At early delay times, these transitions generate hot electrons, depleting conduction-band states and thereby reducing the effective Fermi energy. This transient redistribution of electrons gives rise to several characteristic features in the TA spectrum. First, the lowered Fermi energy shifts the onset of interband transitions to lower energies, producing a pronounced photoinduced absorption (PIA) band centered near 510 nm. Second, modifications to the electronic band structure at higher energies result in a positive spectral feature around 460 nm. Third, partial bleaching of intraband transitions leads to a photobleaching signal at wavelengths longer than approximately 600 nm. At later times, the excess energy of the hot electrons is transferred to the lattice: initially via electron–phonon scattering on a few-picosecond timescale (≈1 ps), followed by lattice heating and expansion over hundreds of picoseconds [40].

Under identical excitation conditions (400 nm excitation), the TA response of the Opal/Au hybrid (Figure 2b) largely reflects that of the gold component. This is expected, since the opal consists of SiO_2 spheres, which do not absorb at 400 nm and thus exhibit no measurable TA signal on their own (see Figure S2). We also observe a weak modulation of the Fabry-Perot oscillations present in the static transmission spectrum of the hybrid structure (see Figure 1d,e), possibly due to a weak, instantaneous refractive index change of the plasmonic coating induced by the pump excitation. Nevertheless, the hybrid sample displays a distinct additional feature—a strong positive signal at approximately 625 nm—coinciding with the opal PBG, where the bare Au film shows negligible response. Fluence-dependence measurements demonstrate that the relative intensity of this band does not depend on the excitation fluence (see Figure S3).

The Opal/Au hybrid is further investigated using angle-resolved TA measurements, which provide insight into the origin of the positive feature observed at 625 nm. This analysis is particularly informative, as purely plasmonic effects are not expected to exhibit angular dispersion. Figure 3 shows the normalized TA spectra of the Opal/Au hybrid recorded 500 fs after excitation at 400 nm, measured with vertically polarized probe at incidence angles of 0°, 20°, 30°, and 45° relative to the normal to the film, represented by blue, green, red, and dark yellow lines, respectively. For reference, the TA spectrum of the bare Au film at normal incidence (0°) under the same excitation conditions is included as a black line. When varying the probe incidence angle, the positive feature in the Opal/Au spectra follows the angular dispersion of the opal PBG as also reported by the static transmission data changing the incident angle (see Figure S4). This trend is further illustrated in the inset of Figure 3, which shows the peak position (circles) as a function of the incident angle together with the theoretical dispersion curve (black line) calculated from the structural parameters of the Opal using the modified Bragg's law for photonic crystals [24, 41]. The direct correspondence between the angular dispersion of the opal PBG and the position of the positive TA band – which at 45° is only sufficient to reduce the amplitude of the negative signal – highlights the photonic contribution to the phenomenon, indicating that it is not purely plasmonic. A non-trivial interplay between the Au NC plasmon and the opal PBG is observed.

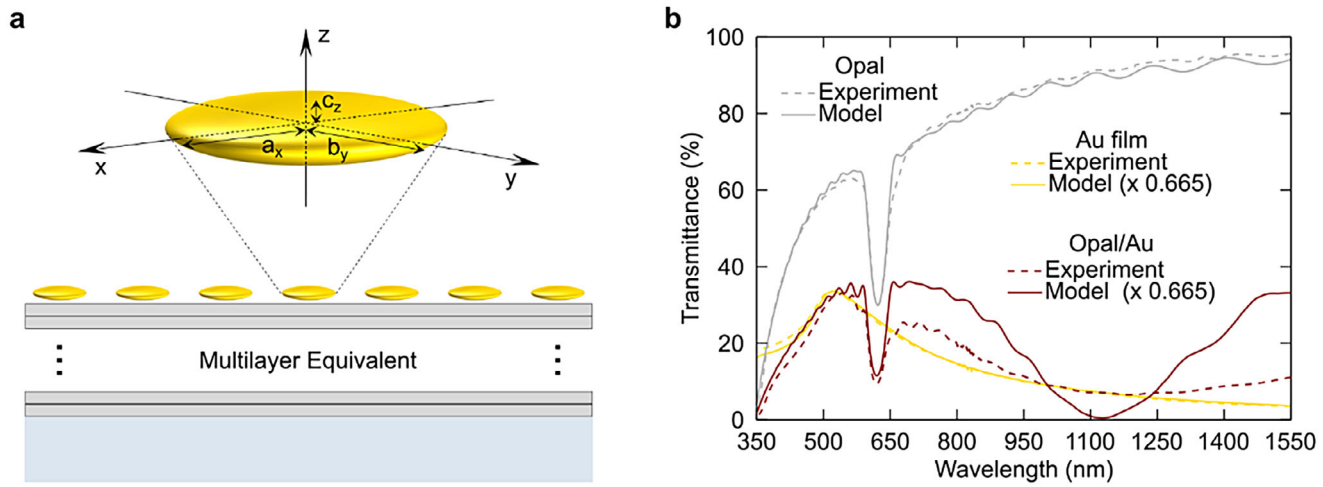

FIGURE 4 | (a) Bottom: Schematic of the modeled Opal/Au hybrid. The 3D opal structure is approximated by a 1D multilayer equivalent, while the Au coating is represented by a layer of oblate Au spheroids dispersed in air. Top: 3D illustration of an oblate spheroid, with a_x, b_y, and c_z denoting the semiaxes along the *x*, *y*, and *z* directions, respectively. (b) Experimental (dashed lines) and simulated (solid lines) transmittance spectra for the Opal (grey), Au film (yellow), and Opal/Au hybrid (dark red) samples.

2.4 | TMM-Based Model of the Opal/Au Hybrid

To elucidate the origin of the photonic-plasmonic interplay observed in the Opal/Au hybrid, we developed an approximate theoretical model based on the TMM model, which is well suited for describing layered structures [42]. In this model, the variation of the dielectric constant ε is considered only along the *z*-axis (see Figure 4a), assuming lateral homogeneity. This represents a reasonable approximation when the analysis is restricted to normal-incidence conditions. The 1D structure was modeled by fitting the experimental transmittance spectra of both the individual constituents and the complete hybrid system.

First, we model the optical response of the Opal alone by building a multilayer equivalent with the opportune refractive index spatial modulation that reproduces the static transmission spectrum (see grey line in Figure 4b). Second, we model the planar Au film (see yellow line in Figure 4b). Finally, we turn to the modeling of the Opal/Au hybrid. In this approach, we aim to theoretically incorporate the Au NC observed via SEM (see Figure 1c), which introduces a plasmonic band centered at around 1100 nm into the optical response of the structure (see Figure 1e).

To construct the 1D model of the Opal/Au hybrid, we place on top of the multilayer equivalent representing the Opal an effective layer characterized by the dielectric constant ε_s of a suspension of oblate gold nano-spheroids in air (see Figure 4a). The value of ε_s is calculated using the Maxwell-Garnett effective medium theory [43].

$$\varepsilon_s = \varepsilon_c \frac{1 + 2\beta\phi}{1 - \beta\phi} \tag{2}$$

where $\varepsilon_c = 1$ is the dielectric function of the continuous medium (air), ϕ is the particles' volume fraction, which is assumed small, and β is the average relative polarizability of the particles calculated as

$$\beta = \frac{\varepsilon_{Au}(\lambda) - \varepsilon_c}{3\{\varepsilon_c + L_i[\varepsilon_{Au}(\lambda) - \varepsilon_c]\}} \tag{3}$$

where L_i are geometrical parameters related to the spheroid semiaxes lengths a_x, b_y, c_z such that $\sum_i L_i = 1$, and $\varepsilon_{Au}(\lambda)$ is gold's dielectric function. Given the symmetry of the opal template, we considered symmetrical spheroids, with $a_x = b_y = mc_z$ where m is a modelling parameter. To better reproduce our experimental data, we found that the best value for m is 8.

The simulated transmittance spectrum of the Opal/Au (Figure 4b, dark red line) closely matches the experimental data. The slight deviations can be attributed to a broader nanostructure size distribution in the sample, yet the overall agreement confirms the reliability of the model for subsequent analysis.

Theoretical insight into the photonic-plasmonic interplay in the Opal/Au hybrid is obtained by analyzing the calculated absorbance A, defined as A = 1–T–R, where T and R denote transmittance and reflectance, respectively. Figure 5a compares the simulated absorbance of an Au film (yellow) on Opal (solid line) and on a flat substrate (dashed line), as well as that of Au NC (dark red) in the two configurations. In both cases, the spectra for Au (film and NC) on Opal clearly exhibits the photonic bandgap (PBG) and Fabry-Pérot oscillations. For Au NC, a broad absorption band associated with the plasmon resonance is also observed. Notably, a pronounced absorption enhancement emerges at the blue edge of the Opal PBG (grey line) for both Au configurations. This enhancement arises on the blue side of the PhCs PBG when it spectrally overlaps with the absorption of the coupled material. Near the PBG edges, the photonic bands flatten, resulting in a substantial reduction of the photon group velocity. The resulting slow-light regime amplifies the interaction between light and the absorbing Au layer at the PhC interface, thereby strengthening the optical response of the hybrid system

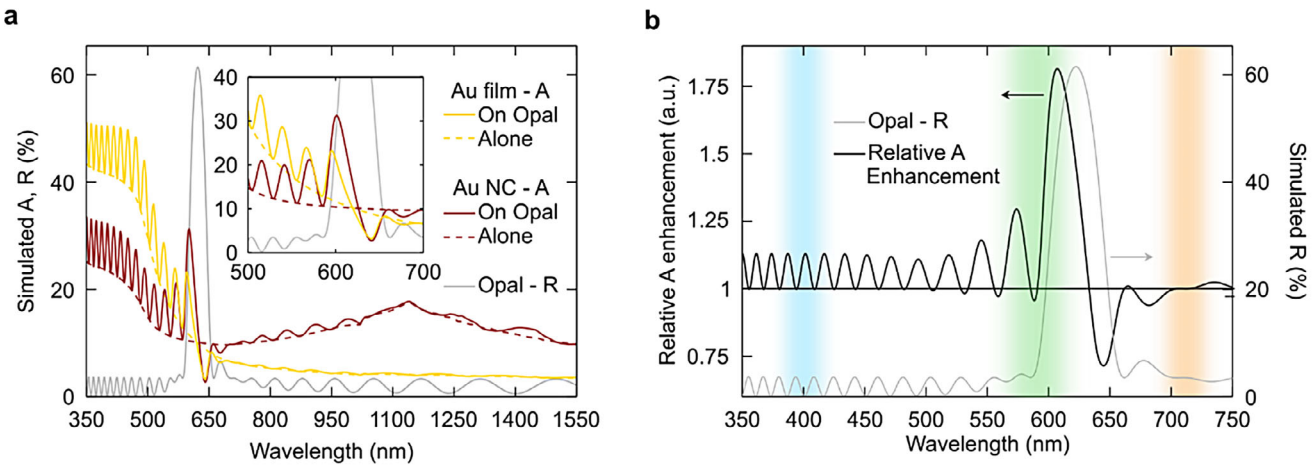

FIGURE 5 | (a) Simulated absorbance spectra of the Au film (yellow) and AuNC (dark red), calculated for structures with (solid lines) and without (dashed lines) the underlying Opal layer. The simulated reflectance of the Opal is shown as a solid grey line. Inset: enlarged view of the absorption enhancement peak at the blue edge of the PBG to highlight the differing enhancement between the Au film and Au NC. (b) Simulated relative absorption enhancement RAE (black line) calculated as $(A^{\text{on Opal}}_{\text{Au NC}}/A_{\text{Au NC}})/(A^{\text{on Opal}}_{\text{Au film}}/A_{\text{Au film}})$. The simulated reflectance spectrum of the Opal is shown in grey. Three different shaded areas are shown.

[44, 45]. While this effect is relatively small for the Au film, it is more pronounced for the Au NC, which exhibits a broad plasmonic absorption centered around 1100 nm with a blue tail extending into the PBG region. The enhanced absorption in the Au nanocaps compared to the Au film can be related to the presence of LSPRs, which strongly amplify the local electromagnetic field. When combined with the slow-light effect at the PBG edge, this field enhancement can lead to a much more pronounced absorption enhancement in the Au nanocaps than in the planar Au film.

The spectral shape of the absorption enhancement provided by the opal PBG can be qualitatively estimated by calculating the ratio $A^{on\ Opal}/A^{on\ substrate}$ for both the Au film and the Au NC. To isolate the additional effects specific to the NC, we normalize their absorption enhancement by that of the film, so that common enhancement effects are effectively removed, leaving the relative absorption enhancement (RAE) of the NC with respect to the film:

$$RAE = \frac{A^{on\ Opal}_{Au\ NC}/A_{Au\ NC}}{A^{on\ Opal}_{Au\ film}/A_{Au\ film}} \quad (4)$$

The RAE, shown in Figure 5b, exhibits a peculiar spectrum, which illustrates that the Au NC experience a wavelength-dependent absorption enhancement relative to the planar film, when coupled to the PhC. Interestingly, the RAE is larger on the blue side of the opal PBG (see the green-shaded area in Figure 5b), is intermediate at lower wavelengths (cyan-shaded area in Figure 5b) and is minimum at longer wavelengths (orange-shaded area in Figure 5b), region where the relative absorption enhancement flattens at unity indicating an equivalent absorption enhancement for the Au NC and the Au film.

2.5 | Excitation Wavelength Dependence of the Transient Spectra

To experimentally verify the wavelength dependence of the RAE, excitation wavelength-dependent TA measurements were performed by tuning the pump to 400 nm (Figure 2), 580 nm, and 710 nm for both the Au film and the Opal/Au hybrid. The three selected wavelengths fall within the regions of intermediate, maximum, and negligible RAE values, as highlighted in Figure 5b.

As shown in Figure S5, the normalized TA spectra of the Au film are independent of the excitation wavelength, confirming that the excitation wavelength-dependent behavior originates primarily from the photonic–plasmonic coupling in the hybrid rather than from the gold itself.

Having established what happens for the bare Au film, Figure 6 compares the normalized TA spectra of the Opal/Au hybrid recorded at 500 fs pump-probe delay following excitation at 580 nm (green) and 710 nm (orange), together with the data previously obtained by exciting at 400 nm (cyan). The spectra are normalized to the peak of the PIA, under the reasonable assumption that this feature originates from the intrinsic response of the Au and is unaffected by the influence of the photonic environment (see Figure 2a). As expected, the relative intensity of the positive peak at the spectral position of the opal PBG is highest for 580 nm excitation, intermediate for 400 nm excitation, and lowest for 710 nm excitation, thus mirroring the RAE spectral behavior (see also Figure S6 for further analysis).

We rationalize these observations by noting that excitation at 580 nm coincides with the region of maximum NC absorption enhancement (see the green-shaded area in Figure 5b), which leads to a stronger transient signal in the metal nanostructures and, consequently, the strongest coupling between the plasmon

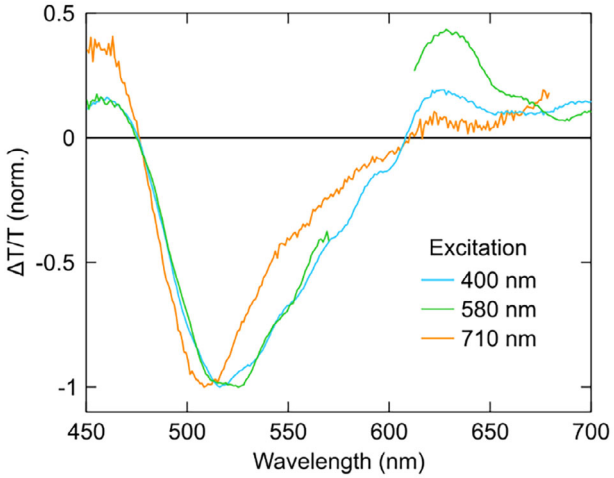

FIGURE 6 | TA spectra at normal incidence taken at 500 fs pump–probe delay after excitation of the Opal/Au hybrid at 400 nm (cyan), 580 nm (green), and 710 nm (orange). The spectra are normalized to the minimum. Data points affected by pump scattering were excluded from the TA spectra at 580 and 710 nm excitation.

and the PBG. By contrast, excitation at 710 nm falls in the spectral region where the RAE is minimum (orange-shaded area in Figure 5b) and excitation at 400 nm within a spectral region where the relative absorption enhancement is intermediate (cyan-shaded area in Figure 5b).

2.6 | Ultrafast Switch for Bacteria Sensing

Finally, the sensing capability of the Opal/Au hybrid was evaluated by comparing femtosecond TA measurements before and after bacterial deposition. Figure 7a shows a SEM image of the hybrid surface after drop-casting a dehydrated *Bacillus Cereus* solution. The bacterial rods, approximately 10 μm in length, are too large to infiltrate the 290 nm opal interstices; thus, their interaction with the hybrid is limited to surface contact. Figure 7b presents the TA spectra recorded at 500 fs pump–probe delay following 400 nm excitation for the hybrid structures with (blue) and without (red) bacterial deposition. The presence of the bacterial analyte clearly modifies the photophysical response, inducing a ≈10 nm transient redshift of the positive bleaching band, also evident in the cw transmission spectra (see Figure S7). This shift may arise from a refractive index change at the air-gold interface due to the presence of bacteria and, as suggested by Paternò et al. [46], from chemical interactions, specifically charge-transfer processes between the bacteria and the nanocaps. The bacteria-induced redshift of the bleaching band modifies the spectral overlap between this feature and the PIA band of bulk Au (Figure 7b), thereby altering the relative weight of these opposing contributions. Figure 7c shows the TA dynamics of the Opal/Au hybrid in the absence (red line) and presence (blue line) of bacteria at 610 nm, where the effect of the redshift on the transient response is most pronounced. In the absence of bacteria, the early dynamics are dominated by a positive bleaching contribution, whereas in their presence, the signal exhibits a dominant negative PIA character, consistent with the modified spectral overlap. This pronounced sign contrast provides a clear optical discriminator between the two conditions. Moreover, in the presence of bacteria, the 610 nm transient signal recovers to positive values within ≈1 ps, consistent with hot-electron cooling in Au, indicating that the system could operate on a picosecond timescale. This behavior demonstrates the capability of the Opal/Au hybrid to translate surface perturbations into distinct transient optical signatures, highlighting its potential as an ultrafast optical biosensing platform.

3 | Conclusion

In conclusion, we conducted a comprehensive investigation of the optical properties of a HCPPC. By combining static optical characterization with femtosecond transient absorption spectroscopy, we elucidated the coupling between plasmonic and photonic features. The experiments, performed under different excitation wavelengths and incidence angles, revealed a pronounced enhancement of the bleaching signal when the plasmon resonance overlaps with the PBG. This enhancement is controlled via the slow-photon effect at the blue edge of the PBG, in excellent agreement with transfer matrix method simulations. As a proof of concept, bacterial deposition on the hybrid surface induced ultrafast optical modulation, demonstrating the sensibility of the system to surface perturbations. These findings position HCPPCs as promising candidates for ultrafast photonic switching and biosensing applications.

4 | Experimental Section/Methods

4.1 | Materials

Thermo Scientific Remel Bacillus Cereus ATCC 11778 Culti-Loops, Difco broth and Corning Dulbecco's Phosphate Buffered Saline (DPBS) were purchased from Fisher (Milan, Italy). Glutaraldehyde solution, Grade I, 25% in H2O, Hexamethyldisilazane reagent grade, ≥99% and ethanol was purchased from Merck Life Science S.r.l. (Milan, Italy).

4.2 | Hybrid Device Preparation and SEM Morphological Characterization

Metallo-dielectric systems were obtained by a two steps processes (i) initially a dielectric colloidal crystals were grown from commercial silica monodisperse microspheres (290 nm diameters) water suspension 10% in volume (Bang Laboratories Inc.; refractive index, nSiO2 = 1.45; standard deviation < 5%) using Vertical Deposition techniques [23]. Then, 20 ± 5 nm of gold thin film was evaporated on the top by e-beam evaporation in high vacuum chamber. Scanning Electron Microscopy (SEM) was used to verify the dimensions of the ordered domains and to characterize the *Bacillus Cereus* strain. The images were obtained using a Helios 5 PFIB CXe (Thermo Fisher Scientific, Waltham, USA) operating at a voltage of 5 kV with in-lens detection. The optical assessment of the hybrid structures was performed using static transmittance measurements with a Varian Cary 5000 double-beam spectrophotometer. Specifically, angular transmittance measurements, ranging from 0∘ to 40°, were conducted by placing the samples on a goniometer with a resolution of 1°.

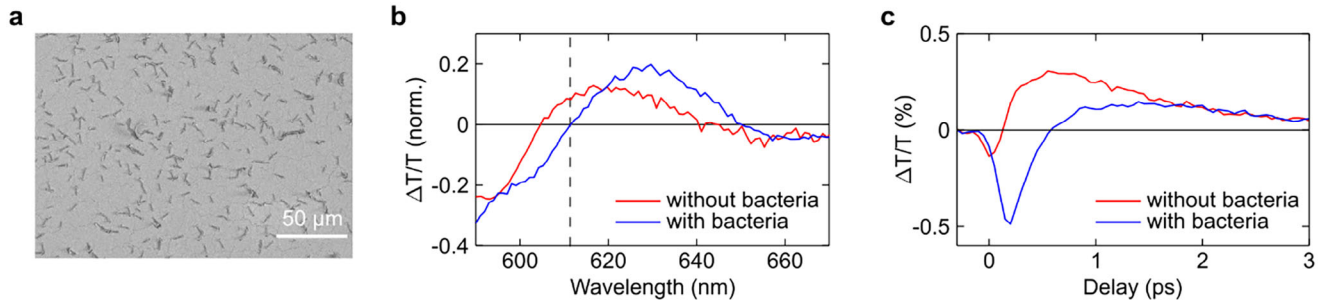

FIGURE 7 | (a) SEM image of the top surface of the Opal/Au sample covered with dehydrated *Bacillus Cereus*. (b) Normalized TA spectra at 500 fs pump–probe delay following 400 nm excitation of the Opal/Au hybrid with (blue line) and without (red line) bacteria in the range between 590 and 670 nm to highlight the redshift upon bacteria deposition. The dashed black line at ≈610 nm represents the spectral position of the dynamics shown in panel c. (c) TA dynamics at ≈610 nm of the Opal/Au sample with (blue line) and without (red line) bacteria.

4.3 | Bacteria Deposition

A bacterial culti-loop is inoculated in Difco broth for 16 h at 37°C. Subsequently, they were harvested by centrifugation (three times 1500 g for 20 min) to eliminate the culture medium and resuspended in DPBS. The desired concentration for the adhesion experiments was reached through consecutive dilutions, and it was evaluated measuring the suspension's turbidity (absorbance = 2 measured at a wavelength of 540 nm) using a V-550 UV/vis spectrophotometer (Jasco Corp., Japan). The bacterial suspension was dropped onto the samples and incubated for two hours at 37°C. After the adhesion experiments, for the SEM analysis and transient absorption measurements, each sample was gently rinsed using DPBS to remove non-adherent bacteria and fixed with 2.5% glutaraldehyde in DPBS at room temperature for 1 h. The sample was subsequently rinsed using DPBS and slowly dehydrated by several passages in ethanol–water solutions for 15 min using increasing concentrations of ethanol (25%; 50%; 75%; 100%), and the dehydration was completed by immersion in hexamethyldisilazane for 30 min.

4.4 | Femtosecond Transient Absorption Spectroscopy

The ultrafast spectroscopy setup was fed by a 150 fs, 2 kHz repetition rate Ti:sapphire system (Libra, Coherent, Santa Clara, CA, USA) with a central wavelength of 800 nm. Transient-absorption measurements were performed by pumping at 400 nm (90 µJ cm^{-2}) with the second harmonic of the laser output, generated with a 1 mm, Type I β-barium borate crystal. The excitation wavelengths at 580 nm (150 µJ cm^{-2}) and at 710 nm (50 µJ cm^{-2}) came from a non-collinear optical parametric amplifier (NOPA). The excitation beam was focused on a circular spot with ~100 µm diameter. The probing pulses, with a spectrum spanning from 450 to 750 nm, were obtained by white-light generation in a 3 mm thick sapphire crystal. The measurements were performed in transmission, and the probe spectrum was detected using a SP2150 Acton, Princeton Instruments spectrometer. The pump beam was modulated by a mechanical chopper at a 1 kHz frequency, and the differential transmission (ΔT/T) spectrum of the probe was measured as a function of probe wavelength and pump–probe delay.

It should be noted that 580 nm does not coincide with the maximum of the RAE (see Figure 5b), which occurs at around 600 nm. This wavelength was chosen to ensure that the region containing the most significant signal remains unaffected by pump scattering.

4.5 | TMM Model

The opals were modeled by a periodic layered structure with period $d = D\sqrt{\frac{2}{3}}$ (corresponding to the interplanar spacing of the (1,1,1) planes) made by 17 layers, where each layer had a spatially modulated refractive index (see Figure S8)

$$n(z,\lambda) = n_{ave}(\lambda) + \Delta(\lambda)\cos\left(2\pi\frac{z}{d}\right) - i\eta(\lambda),\ -\frac{d}{2} \le z \le \frac{d}{2}$$

$$n_{ave}(\lambda) = f\, n_{SiO_2}(\lambda) + (1-f)$$

$$\Delta(\lambda) = c\, n_{SiO_2}(\lambda) \tag{5}$$

Given the fcc structure, the filling factor f was 0.74. The term $-i\eta(\lambda)$ was an effective absorption term used to model the scattering, by fitting the experimental transmission with a polynomial interpolant far from the PhC resonance; the c factor had then been determined by fitting the transmission of the whole PhC structure (see Figure S9 for the fit).

The Au film was modeled as a single layer of gold with 18 nm thickness, in agreement with the nominal thickness measured experimentally.

Acknowledgements

This research was supported by Consiglio Nazionale delle Ricerche Progetti@CNR EPOCALE. D.F. acknowledges the support under the National Recovery and Resilience Plan (NRRP), Mission 4 Component 2 Investment 1.4 – Call for tender No. 3138 of December 16, 2021 of the Italian Ministry of University and Research, funded by the European Union –

NextGenerationEU [Award Number: CNMS named MOST, Concession Decree No. 1033 of June 17, 2022, adopted by the Italian Ministry of University and Research, CUP: B43C22000440001, Spoke 14 "'Hydrogen and New Fuels"']. Open access publishing facilitated by Consiglio Nazionale delle Ricerche, as part of the Wiley - CRUI-CARE agreement.

Funding

Consiglio Nazionale delle Ricerche Progetti@CNR EPOCALE; The National Recovery and Resilience Plan (NRRP), Mission 4 Component 2 Investment 1.4 – Call for tender No. 3138 of December 16, 2021 of the Italian Ministry of University and Research, funded by the European Union – NextGenerationEU [Award Number: CNMS named MOST, Concession Decree No. 1033 of June 17, 2022, adopted by the Italian Ministry of University and Research, CUP: B43C22000440001, Spoke 14 "'Hydrogen and New Fuels"']. Open access publishing facilitated by Consiglio Nazionale delle Ricerche, as part of the Wiley - CRUI-CARE agreement.

Conflicts of Interest

The authors declare no conflicts of interest.

Data Availability Statement

The data are available from the authors upon request.

References

1. D. Gao, W. Ding, M. Nieto-Vesperinas, et al., "Optical Manipulation From the Microscale to the Nanoscale: Fundamentals, Advances and Prospects," *Light: Science & Applications* 6 (2017): 17039, https://doi.org/10.1038/lsa.2017.39.

2. E. De Tommasi, E. Esposito, S. Romano, et al., "Frontiers of Light Manipulation in Natural, Metallic, and Dielectric Nanostructures," *Rivista del Nuovo Cimento* 44, no. 7 (2021): 1–68, https://doi.org/10.1007/s40766-021-00015-w.

3. M. Frimmer and L. Novotny, "Controlling Light at the Nanoscale," *Europhysics News* 46, no. 5-6 (2015): 27–30, https://doi.org/10.1051/epn/2015504.

4. Y. Yang, J. Seong, M. Choi, et al., "Integrated Metasurfaces for Re-Envisioning a Near-Future Disruptive Optical Platform," *Light: Science & Applications* 12 (2023): 152, https://doi.org/10.1038/s41377-023-01169-4.

5. X. Bao, S. Yu, W. Lu, et al., "Tunable High-Sensitivity Four-Frequency Refractive Index Sensor Based on Graphene Metamaterial," *Sensors* 24, no. 8 (2024): 2658, https://doi.org/10.3390/s24082658.

6. C.-T. C. Chou, Y.-F. Chou Chau, H. J. Huang, et al., "Highly Sensitive and Tunable Plasmonic Sensor Based on a Nanoring Resonator With Silver Nanorods," *Nanomaterials* 10, no. 7 (2020): 1399, https://doi.org/10.3390/nano10071399.

7. E. Yablonovitch, "Photonic Band-Gap Crystals," *Journal of Physics: Condensed Matter* 5 (1993): 2443, https://doi.org/10.1088/0953-8984/5/16/004.

8. S. E. Skipetrova, "Finite-Size Scaling of the Density of States Inside Band Gaps of Ideal and Disordered Photonic Crystals," *The European Physical Journal B* 93 (2020): 70, https://doi.org/10.1140/epjb/e2020-100473-3.

9. S. B. Hasan, A. P. Mosk, W. L. Vos, and A. Lagendijk, "Finite-Size Scaling of the Density of States in Photonic Band Gap Crystals," *Physical Review Letters* 120 (2018): 237402, https://doi.org/10.1103/PhysRevLett.120.237402.

10. M. P. Mcoyi, K. T. Mpofu, M. Sekhwama, and P. Mthunzi-Kufa, "Developments in Localized Surface Plasmon Resonance," *Plasmonics* 20 (2024): 5481–5520, https://doi.org/10.1007/s11468-024-02620-x.

11. K. Kant, R. Beeram, Y. Cao, et al., "Plasmonic Nanoparticle Sensors: Current Progress, Challenges, and Future Prospects," *Nanoscale Horizons* 9 (2024): 2085–2166, https://doi.org/10.1039/D4NH00226A.

12. N. J. Halas, S. Lal, W.-S. Chang, S. Link, and P. Nordlander, "Plasmons in Strongly Coupled Metallic Nanostructures," *Chemical Reviews* 111, no. 6 (2011): 3913–3961, https://doi.org/10.1021/cr200061k.

13. H. Yu, Y. Peng, Y. Yang, and Z. Y. Li, "Plasmon-Enhanced Light–Matter Interactions and Applications," *npj Computational Materials* 5 (2019): 45, https://doi.org/10.1038/s41524-019-0184-1.

14. V. Giannini, A. I. Fernández-Domínguez, S. C. Heck, and S. A. Maier, "Plasmonic Nanoantennas: Fundamentals and Their Use in Controlling the Radiative Properties of Nanoemitters," *Chemical Reviews* 111, no. 6 (2011): 3888–3912, https://doi.org/10.1021/cr1002672.

15. J. A. Schuller, E. S. Barnard, W. Cai, Y. C. Jun, J. S. White, and M. L. Brongersma, "Plasmonics for Extreme Light Concentration and Manipulation," *Nature Materials* 9 (2010): 193–204, https://doi.org/10.1038/nmat2630.

16. R. K. Gangwar, A. K. Pathak, and S. Kumar, "Recent Progress in Photonic Crystal Devices and Their Applications: A Review," *Photonics* 10, no. 11 (2023): 1199, https://doi.org/10.3390/photonics10111199.

17. S. G. Romanov, A. V. Korovin, A. Regensburger, and U. Peschel, "Hybrid Colloidal Plasmonic-Photonic Crystals," *Advanced Materials* 23, no. 22 (2011): 2515–2533, https://doi.org/10.1002/adma.201100460.

18. P. Lalanne, W. Yan, K. Vynck, C. Sauvan, and J.-P. Hugonin, "Light Interaction With Photonic and Plasmonic Resonances," *Laser & Photonics Reviews* 12, no. 3 (2018): 1700113, https://doi.org/10.1002/lpor.201700113.

19. C. Farcau, "Linear Arrays of Metal-Coated Microspheres: A Polarization-Sensitive Hybrid Colloidal Plasmonic–Photonic Crystal," *The European Physical Journal Plus* 138 (2023): 1000, https://doi.org/10.1140/epjp/s13360-023-04638-2.

20. A. I. Vanina, Y. A. Kumzerov, S. G. Romanov, and V. G. Solovyev, "Transmission and Conversion of Electromagnetic Radiation by Photonic Crystal Metal–Dielectric Systems Based on Opals," *Optics and Spectroscopy* 128, no. 12 (2020): 2022–2027, https://doi.org/10.1134/S0030400x20121078.

21. L. Li and H. Hao, "Evolution of High-Order Tamm Plasmon Modes With a Metal-PhC Cavity," *Scientific Reports* 12 (2022): 14921, https://doi.org/10.1038/s41598-022-19435-7.

22. R. Mudi, S. Mallik, B. Veeraghattam, D. K. Goswami, B. N. S. Bhaktha, and K. Debnath, "Morphology Dependent Excitation of Hybrid Tamm-Bandedge State in Metal Coated Opal Three-Dimensional Photonic Crystal," *Optical Materials* 140 (2023): 113848, https://doi.org/10.1016/j.optmat.2023.113848.

23. R. Mudi, A. Carpentiero, M. Bollani, et al., "Inverse Opal Optical Tamm State for Sensing Applications," *Photonics and Nanostructures—Fundamentals and Applications* 62 (2024): 101315, https://doi.org/10.1016/j.photonics.2024.101315.

24. S. Bo, H. Lu, S. Shi, D. Li, and J. Zhao, "Experimental Demonstration of Coupling Between Cavity Resonance and Tamm Plasmons in Photonic Multilayers," *Optics Express* 32, no. 22 (2024): 39108–39116, https://doi.org/10.1364/OE.540009.

25. V. Robbiano, M. Giordano, C. Martella, et al., "Hybrid Plasmonic–Photonic Nanostructures: Gold Nanocrescents Over Opals," *Advanced Optical Materials* 1, no. 5 (2013): 389–396, https://doi.org/10.1002/adom.201200060.

26. S. Sarkar, A. K. Ghosh, M. Adnan, et al., "Enhanced Figure of Merit via Hybridized Guided-Mode Resonances in 2D-Metallic Photonic Crystal Slabs," *Advanced Optical Materials* 10, no. 22 (2022): 2200954, https://doi.org/10.1002/adom.202200954.

27. R. Hatsuoka, K. Yamasaki, K. Wada, T. Matsuyama, and K. Okamoto, "Tunable Plasmon Resonance in Silver Nanodisk-On-Mirror Structures and Scattering Enhancement by Annealing," *Nanomaterials* 14, no. 19 (2024): 1559, https://doi.org/10.3390/nano14191559.

28. S. Guddala, S. A. Kamanoor, A. Chiappini, M. Ferrari, and N. R. Desai, "Experimental Investigation of Photonic Band Gap Influence on Enhancement of Raman-Scattering in Metal-Dielectric Colloidal

Crystals," *Journal of Applied Physics* 112 (2012): 084303, https://doi.org/10.1063/1.4758315.

29. D. Wang, X. Zhao, X. Liu, Z. Mu, and Z. Gu, "Rapid Identification of Electricigens via Silver-Plated Photonic Crystal Filters," *Nano Research* 9, no. 9 (2016): 2760–2771, https://doi.org/10.1007/s12274-016-1164-0.

30. M. Toma, Y. Itakura, S. Namihara, and K. Kajikawa, "Sensitive Label-Free Immunoassay by Colorimetric Plasmonic Biosensors Using Silver Nanodome Arrays," *Advanced Engineering Materials* 25 (2023): 2200912, https://doi.org/10.1002/adem.202200912.

31. Z. Yu, K. Zhao, Y. Zhao, Q. Feng, and C. Ye, "Hybrid SPR/Fabry–Pérot Cavity-Based Films With Versatile Color Tunability and Sensitive Environmental Sensing," *Nano Letters* 25, no. 22 (2025): 10634–10640, https://doi.org/10.1021/acs.nanolett.5c02393.

32. N. Del Fatti and F. Vallée, "Ultrafast Optical Nonlinear Properties of Metal Nanoparticles," *Applied Physics B: Lasers and Optics* 73, no. 4 (2001): 383–390, https://doi.org/10.1007/s003400100648.

33. F. Hudelist, R. Buczynski, A. J. Waddie, and M. R. Taghizadeh, "Design and Fabrication of Nano-Structured Gradient Index Microlenses," *Optics Express* 17, no. 5 (2009): 3255–3263, https://doi.org/10.1364/OE.17.003255.

34. J. N. Acharyya, N. R. Desai, R. B. Gangineni, and G. V. Prakas, "Photonic Cavity-Mediated Tunable Ultrafast Absorption Dynamics in $BaTiO_3$-Based One-Dimensional Photonic Crystal," *ACS Applied Electronic Materials* 3, no. 4 (2021): 1904–1911, https://pubs.acs.org/doi/10.1021/acsaelm.1c00142.

35. Y. Kurokawa and H. T. Miyazaki, "Metal-Insulator-Metal Plasmon Nanocavities: Analysis of Optical Properties," *Physical Review B* 75, no. 3 (2007): 035411, https://doi.org/10.1103/PhysRevB.75.035411.

36. V. Morandi, F. Marabelli, V. Amendola, M. Meneghetti, and D. Comoretto, "Colloidal Photonic Crystals Doped With Gold Nanoparticles: Spectroscopy and Optical Switching Properties," *Advanced Functional Materials* 17 (2007): 2779, https://doi.org/10.1002/adfm.200600764.

37. B. Ding, M. E. Pemble, A. V. Korovin, U. Peschel, and S. G. Romanov, "Three-Dimensional Photonic Crystals With an Active Surface: Gold Film Terminated Opals," *Physical Review B* 82, no. 3 (2010): 035119, https://doi.org/10.1103/PhysRevB.82.035119.

38. C. Charnay, A. Lee, S.-Q. Man, et al., "Reduced Symmetry Metallodielectric Nanoparticles: Chemical Synthesis and Plasmonic Properties," *The Journal of Physical Chemistry B* 107, no. 30 (2003): 7327–7333, https://doi.org/10.1021/jp034309r.

39. A. I. Maaroof, M. B. Cortie, N. Harris, and L. Wieczorek, "Mie and Bragg Plasmons in Subwavelength Silver Semi-Shells," *Small* 4, no. 12 (2008): 2292–2299, https://doi.org/10.1002/smll.200800203.

40. X. Zhang, M. Wang, F. Tang, et al., "Transient Electronic Depletion and Lattice Expansion Induced Ultrafast Band Edge Plasmons," *Advanced Science* 7, no. 2 (2019): 1902408, https://doi.org/10.1002/advs.201902408.

41. S.-H. Kim, S. Y. Lee, S.-M. Yang, and G.-R. Yi, "Self-Assembled Colloidal Structures for Photonics," *NPG Asia Materials* 3 (2011): 25–33, https://doi.org/10.1038/asiamat.2010.192.

42. F. L. Pedrotti, L. S. Pedrotti, and L. M. Pedrotti, in*Introduction to Optics* (Cambridge University Press, 2017), https://doi.org/10.1017/9781108552493.

43. K. J. Frankforter, D. C. Ludois, and D. J. Klingenberg, "Dielectric Nanoparticle Suspensions for Increased Electrostatic Forces," *Journal of Applied Physics* 131, no. 4 (2022): 044701, https://doi.org/10.1063/5.0078551.

44. T. Baba, "Slow Light in Photonic Crystals," *Nature Photonics* 2 (2008): 465–473, https://doi.org/10.1038/nphoton.2008.146.

45. M. Notomi, "Manipulating Light With Strongly Modulated Photonic Crystals," *Reports on Progress in Physics* 73, no. 9 (2010): 096501, https://doi.org/10.1088/0034-4885/73/9/096501.

46. G. M. Paternò, L. Moscardi, S. Donini, et al., "Hybrid One-Dimensional Plasmonic–Photonic Crystals for Optical Detection of Bacterial Contaminants," *The Journal of Physical Chemistry Letters* 10, no. 17 (2019): 4980–4986, https://doi.org/10.1021/acs.jpclett.9b01612.

Supporting Information

Additional supporting information can be found online in the Supporting Information section.

Supporting File: adom71135-sup-0001-SuppMat.docx.